

Towards a more robust non-invasive assessment of functional connectivity

Britta U. Westner^{1*}, Jan Kujala², Joachim Gross³, Jan-Mathijs Schoffelen¹

Affiliations:

1. Radboud University, Donders Institute for Brain, Cognition and Behaviour, Nijmegen, The Netherlands
2. Department of Psychology, University of Jyväskylä, Jyväskylä, Finland
3. Institute for Biomagnetism and Biosignal Analysis, University of Münster, Münster, Germany

* Corresponding author, britta.westner@donders.ru.nl

1 Abstract

2 Non-invasive evaluation of functional connectivity, based on source-reconstructed estimates
3 of phase-difference-based metrics, is notoriously non-robust. This is due to a combination of
4 factors, ranging from a misspecification of seed regions to suboptimal baseline assumptions, and
5 residual signal leakage. In this work, we propose a new analysis scheme of source level phase-
6 difference-based connectivity, which is aimed at optimizing the detection of interacting brain
7 regions. Our approach is based on the combined use of sensor subsampling and dual-source
8 beamformer estimation of all-to-all connectivity on a prespecified dipolar grid. First, a pairwise
9 two-dipole model, to account for reciprocal leakage in the estimation of the localized signals,
10 allows for a usable approximation of the pairwise bias in connectivity due to residual leakage
11 of ‘third party’ noise. Secondly, using sensor array subsampling, the recreation of multiple
12 connectivity maps using different subsets of sensors allows for the identification of consistent
13 spatially localized peaks in the 6-dimensional connectivity maps, indicative of true brain region
14 interactions. These steps are combined with the subtraction of null coherence estimates to
15 obtain the final coherence maps. With extensive simulations, we compared different analysis
16 schemes for their detection rate of connected dipoles, as a function of signal-to-noise ratio,

17 phase difference and connection strength. We demonstrate superiority of the proposed analysis
18 scheme in comparison to single-dipole models, or an approach that discards the zero phase
19 difference component of the connectivity. We conclude that the proposed pipeline allows for
20 a more robust identification of functional connectivity in experimental data, opening up new
21 possibilities to study brain networks with mechanistically inspired connectivity measures in
22 cognition and in the clinic.

23 **1 Introduction**

24 The brain is considered to operate as a network of interacting, functionally specialized regions.
25 The development and application of analysis tools to probe those interactions in the healthy
26 human brain from non-invasive electrophysiological measurements has been an active area of
27 research in the past few decades. Part of that work is grounded in the notion that interre-
28 gional interactions may be reflected by statistical dependencies between band-limited signal
29 components that can be picked up from locally activated brain areas. One way to quantify this
30 so-called functional connectivity is to estimate some measure of relative phase consistency or
31 phase synchrony (Varela et al., 2001), for instance using the coherence coefficient, or a derived
32 metric (Bastos and Schoffelen, 2016). From a mechanistic point of view it has been hypoth-
33 esized that consistent phase differences of oscillatory processes facilitate neuronal interactions
34 by virtue of a mutual temporal alignment of cycles of increased neuronal excitability (Fries,
35 2005, 2015; Bonnefond et al., 2017). In sum, connectivity estimates based on phase synchrony
36 are a valuable metric in cognitive neuroscience.

37 It is commonly agreed that, for interpretability, connectivity estimates should be assessed
38 at the source level. This is because connectivity estimates are invariably confounded by spatial
39 leakage (Schoffelen and Gross, 2009). Promising work from the early 2000s developed (Gross et
40 al., 2001) and successfully applied (*e.g.*, Pollok et al., 2005; Schoffelen et al., 2005) the Dynamic
41 Imaging of Coherent Sources (DICS) technique, a frequency domain version of a beamformer
42 for source reconstruction, to identify networks of phase synchronized brain regions based on
43 the strong physiological periodicities during smooth finger movements in healthy participants.
44 Further studies focused on synchrony at the frequency of Parkinsonian or essential tremor in
45 clinical populations (Timmermann et al., 2003; Pollok et al., 2004). In the decades following

46 this early work, the research community has also started studying envelope correlations of
47 band-limited signals instead of phase synchrony. This latter metric has been successfully used
48 to identify properties of networks predominantly during the brain's resting state, yielding a
49 body of literature with well interpretable and consistent findings (Brookes et al., 2011; Hipp et
50 al., 2012; Baker et al., 2014; Colclough et al., 2016; de Pasquale et al., 2016). Despite ongoing
51 methodological work to improve source reconstruction (Dalal et al., 2006; Woolrich et al., 2011;
52 Hillebrand et al., 2012; Nunes et al., 2020; Kuznetsova et al., 2021) and novel phase synchrony
53 based connectivity metrics (Aviyente et al., 2011; Vinck et al., 2011; Ghanbari and Moradi,
54 2020), neuroscientific findings employing phase synchrony seem to be more scarce and less
55 consistent (Colclough et al., 2016; O'Neill et al., 2018).

56 Assuming that metrics based on phase differences tap into fundamental mechanisms of
57 brain organization and communication (Fries, 2005, 2015; Bonnefond et al., 2017), then why
58 is it seemingly so difficult to find converging evidence across studies? One reason for this
59 might be that the methodological adversities are larger than commonly assumed (Bastos and
60 Schoffelen, 2016; Palva et al., 2018; He et al., 2019). One of those difficulties is spatial leakage,
61 both from second party and third party sources, which renders the lower bound of the true
62 connectivity unknown. Proposed techniques for leakage correction, on the other hand, might
63 be too aggressive and also compromise or even remove the signal of interest. Furthermore,
64 data quality might further impede the reliable estimation of phase difference: low signal-to-
65 noise ratio (SNR) might hinder the reliable identification of seed regions of interest, while SNR
66 differences across conditions occlude the interpretation of connectivity, since the estimation of
67 phase-based connectivity measures is sensitive to SNR changes.

68 In this paper, we propose a new method that tackles these problems. We propose to address
69 the issue of suboptimal region of interest (ROI) or seed selection through consideration of the full
70 6-dimensional all-to-all connectivity source space, using a two-dipole constraint beamformer.
71 We further propose an estimation of the null coherence which approximates the bias in the
72 coherence estimate and can be used to correct the output. Finally, we reduce estimation bias
73 by aggregating over the results of many source reconstructions using sensor array subsampling,
74 thereby creating a more stable and robust estimate.

75 In the following, we will first introduce beamforming for source reconstruction and explain

76 the problem of spatial leakage in more detail. Then we will line out the components of our
77 proposed beamforming approach.

78 1.1 Beamformers for source reconstruction

79 Non-invasive electrophysiological measurements (electric potential differences for electroen-
80 cephalography (EEG) or magnetic fields (gradients) for magnetoencephalography (MEG)) re-
81 flect a mixture of the temporal activation profiles from neural and non-neural sources. To
82 disentangle the individual contributions of each of those sources to the spatiotemporal mixture
83 in the observed signals, source reconstruction techniques can be applied. These techniques
84 have developed into a valuable tool for the analysis of non-invasive electrophysiological signals
85 obtained during cognitive experiments. Solving the so-called inverse problem by combining
86 a forward model with additional assumptions, source reconstruction techniques aim to build
87 models of the spatiotemporal characteristics of the neural generators that underlie the mea-
88 sured signals, unmixing the observed channel-level data. The biologically plausible forward
89 model (or gain matrix) describes the spatial distribution of the observed signals, typically for
90 a set of equivalent current dipole sources. The additional model assumptions are necessary
91 to constrain the number of solutions to the inverse problem, which in principle are unlimited.
92 Adaptive beamformers are a class of source reconstruction techniques that do not a priori make
93 explicit assumptions with respect to the number or location of active sources, but rather assume
94 the underlying sources to be temporally uncorrelated. Usually, for each of a set of predefined
95 source locations, a spatial filter is constructed under two constraints: 1) a unit gain constraint,
96 which means that it should pass on all of the activity that originates from that specific loca-
97 tion, and 2) a minimum variance constraint, which minimizes the variance of the reconstructed
98 activity at each location. Mathematically, this linearly constrained minimum variance (LCMV;
99 [Van Veen et al., 1997](#)) spatial filter is computed as follows:

$$\mathbf{w}^\top(r) = [\mathbf{h}^\top(r)\mathbf{C}^{-1}\mathbf{h}(r)]^{-1}\mathbf{h}^\top(r)\mathbf{C}^{-1} , \quad (1)$$

100 where $\mathbf{w}(r)$ is the spatial filter at source location r and \top refers to the transpose operation.
101 $\mathbf{h}(r)$ is the source location-specific gain vector (which can be thought of as a spatial fingerprint),
102 and \mathbf{C}^{-1} is the mathematical inverse of the channel covariance matrix. As an alternative to

103 the channel level covariance matrix, one can use a complex-valued cross-spectral density (CSD)
104 matrix, based on the channel Fourier coefficients for a given frequency bin, resulting in the
105 DICS algorithm (Gross et al., 2001).

106 Beamformers have gained prominence as one of the most popular source reconstruction
107 techniques because they typically provide relatively robust reconstructions of neural activity
108 without the need of sophisticated parameter tweaking (Westner et al., 2022). However, some
109 limiting factors exist with respect to functional connectivity. In the following, we will present the
110 typical distortions when source reconstructing functional connectivity, as well as our approach
111 to mitigate these.

112 1.2 The effect of signal leakage on source connectivity estimates

113 In the context of connectivity estimation, an important concept is that of signal leakage. This
114 refers to the fact that each location’s estimated activity reflects an unknown mixture of the
115 true activity at this location and signal contributions from distant noise sources of both neural
116 and non-neural origin. Mathematically, this can be shown as detailed below.

117 Considering the generative model of the sensor-level data, the sensor signals reflect a sum-
118 mation of the underlying source signals, each multiplied by their spatial fingerprint:

$$\mathbf{X} = \sum_{i=1}^I \mathbf{h}(r_i, q_i) \mathbf{s}_i + \mathbf{N} . \quad (2)$$

119 Here, \mathbf{X} is a number-of-channels by number-of-observations matrix with complex-valued
120 Fourier coefficients, \mathbf{h} is the gain vector for a dipolar source at location r_i and with orientation
121 q_i , and \mathbf{s}_i is a 1 by number-of-observations source activity vector, here assumed to be complex-
122 valued, *i.e.*, to reflect both amplitude and phase for the observations. \mathbf{N} is a number-of-channels
123 by number-of-observations matrix, reflecting the non-brain noise in the measured data.

124 Assume that we have computed a pair of spatial filters, \mathbf{w}_1 and \mathbf{w}_2 , and we use these
125 spatial filters to compute an estimate of the source level Fourier coefficients: $\hat{\mathbf{s}}_1 = \mathbf{w}_1^\top \mathbf{X}$, and
126 $\hat{\mathbf{s}}_2 = \mathbf{w}_2^\top \mathbf{X}$. From these estimates one can compute a connectivity metric, for instance the
127 coherence coefficient, for this dipole pair:

$$coh = \frac{|\hat{\mathbf{s}}_1 \hat{\mathbf{s}}_2^H|}{\sqrt{(\hat{\mathbf{s}}_1 \hat{\mathbf{s}}_1^H)(\hat{\mathbf{s}}_2 \hat{\mathbf{s}}_2^H)}} , \quad (3)$$

128 where \mathbf{H} denotes the conjugate transposition. Note that for simplicity of notation, we omit
 129 the scaling with the number of observations, which drops out of the equation anyhow. We
 130 also note that a non-zero numerator in the equation above suggests linear dependence between
 131 the estimated sources 1 and 2. Below, we inspect this quantity, *i.e.*, the cross-spectral density
 132 estimate between the two sources, in more detail.

133 For the given pair of dipoles, and considering the data model $\mathbf{X} = \mathbf{h}_1 \mathbf{s}_1 + \mathbf{h}_2 \mathbf{s}_2 + \mathbf{N}$ with \mathbf{N}
 134 now reflecting all signal contributions to the observed data that are not originating from the
 135 two dipole pairs-of-interest, we can express the cross-spectral density estimate between the two
 136 dipoles as:

$$\begin{aligned} \hat{\mathbf{s}}_1 \hat{\mathbf{s}}_2^H &= (\mathbf{w}_1^\top \mathbf{X})(\mathbf{w}_2^\top \mathbf{X})^H \\ &= (\mathbf{w}_1^\top (\mathbf{h}_1 \mathbf{s}_1 + \mathbf{h}_2 \mathbf{s}_2 + \mathbf{N}))(\mathbf{w}_2^\top (\mathbf{h}_1 \mathbf{s}_1 + \mathbf{h}_2 \mathbf{s}_2 + \mathbf{N}))^H . \end{aligned} \quad (4)$$

137 Introducing g_{ij} as a scalar value that results from computing the inner product between
 138 spatial filter \mathbf{w}_i and gain vector \mathbf{h}_j and which reflects the filter's gain at location i for a source
 139 originating from location j , we obtain:

$$\hat{\mathbf{s}}_1 \hat{\mathbf{s}}_2^H = (g_{11} \mathbf{s}_1 + g_{12} \mathbf{s}_2 + \mathbf{w}_1^\top \mathbf{N})(g_{21} \mathbf{s}_1 + g_{22} \mathbf{s}_2 + \mathbf{w}_2^\top \mathbf{N})^H . \quad (5)$$

140 When using an inverse algorithm with a typical unit-gain constraint, $\mathbf{w}_i^\top \mathbf{h}_i = g_{ii} = 1$, the
 141 above further reduces to:

$$\begin{aligned} \hat{\mathbf{s}}_1 \hat{\mathbf{s}}_2^H &= (\mathbf{s}_1 + g_{12} \mathbf{s}_2 + \mathbf{w}_1^\top \mathbf{N})(g_{21} \mathbf{s}_1 + \mathbf{s}_2 + \mathbf{w}_2^\top \mathbf{N})^H \\ &= (\mathbf{s}_1 + g_{12} \mathbf{s}_2)(g_{21} \mathbf{s}_1 + \mathbf{s}_2)^H + (\mathbf{s}_1 + g_{12} \mathbf{s}_2) \mathbf{N}^H \mathbf{w}_2 + \mathbf{w}_1^\top \mathbf{N} (g_{21} \mathbf{s}_1 + \mathbf{s}_2)^H + \mathbf{w}_1^\top \mathbf{N} \mathbf{N}^H \mathbf{w}_2 . \end{aligned} \quad (6)$$

142 In other words, for a given dipole pair, the estimated cross-spectral density between two
 143 sources does not only depend on the sources' true cross-spectral density, but is also affected by:

- 144 1. signal leakage from the other dipole-of-interest, specifically when g_{12} and g_{21} are non-
 145 negligible, *cf.* the leftmost term in the above equation

- 146 2. the interaction between the noise, projected through the spatial filter, and the sources'
147 activity, *cf.* the middle two terms in the above equation
- 148 3. the interaction between the projected noise at the location of the dipoles, *cf.* the rightmost
149 term in the above equation

150 Note, that the above reasoning is independent of the exact inverse algorithm used. The
151 different types of leakage will also affect the estimates of the individual dipoles' power. Leakage
152 will always cause misestimation of metrics that are derived from the estimated source level
153 quantities. This also applies to spatial maps of connectivity, which are typically constructed
154 using a limited number of predefined seed dipole locations. Local maxima in these spatial maps
155 (which are either expressed as a difference between two experimental conditions or in relation
156 to a baseline) are then interpreted as regions that are functionally connected to the seed dipole.
157 Irrespective of the specific connectivity metric used, spatial structure in these maps due to
158 leakage may lead to inference of false positive connections. Furthermore, true connections may
159 be missed altogether, if the seed dipoles have been misspecified by the researcher.

160 1.3 Alleviating the effect of leakage

161 In order to address some of the problems associated with leakage, it has been proposed to use
162 connectivity metrics that disregard the interaction along the real-valued axis (*e.g.*, the imagi-
163 nary part of coherency (Nolte et al., 2004) or the multivariate interaction measure (MIM, Ewald
164 et al., 2012)), or to remove the instantaneous leakage originating from one or more dipoles prior
165 to estimating the connectivity on the residuals (Brookes et al., 2012; Hipp et al., 2012; Col-
166 clough et al., 2015; Wens et al., 2015). Although these adjustments avoid an overinterpretation
167 of leakage-affected findings, the sensitivity to true signal interactions at small phase differences
168 is diminished. In addition, these leakage correction schemes do not eliminate the necessity to
169 statistically evaluate the estimated connectivity against a well-defined null hypothesis. This
170 step is usually not straightforward since an appropriate baseline is not available: either because
171 of differences in the signal specific to condition or subject group (see *e.g.*, Bastos and Schof-
172 felen, 2016), or because of the absence of a baseline condition altogether (*e.g.*, in single group
173 resting-state studies). Finally, in a context where seed-based connectivity maps are evaluated,
174 there is no guarantee that the seed regions have been appropriately specified.

175 In this work, we propose an analysis scheme of source level connectivity (here expressed as
176 the coherence coefficient), accounting as much as possible for the effects of leakage but without a
177 reduction in sensitivity for true interactions at small phase differences. Moreover, we will derive
178 estimates of a usable lower bound of the estimated coherence between dipole pairs, which can be
179 used as a correction to more accurately evaluate spatial maps of connectivity, thus avoiding the
180 issues associated with inappropriate or absent baseline conditions. Using extensive simulations,
181 we show superiority of our analysis scheme in comparison to other approaches.

182 1.4 Proposed analysis approach

183 The analysis approach we outline in this paper consists of several elements: We make use of
184 a two-dipole constraint beamformer (Dalal et al., 2006; Brookes et al., 2007; Schoffelen et al.,
185 2008; Moiseev et al., 2011), approximate and correct for the estimated bias due to noise leakage,
186 and embed the approach in a sensor array subsampling scheme. Below, we will discuss all those
187 elements in more detail.

188 **Two-dipole constraint beamformer and bias estimate** The approach is based on an all-
189 to-all approach, where coherence is estimated between all pairs of beamformer reconstructed
190 dipoles defined on an evenly spaced 3-dimensional grid, covering the entire brain. Using a
191 two-dipole constraint in a beamformer formulation, we compute pairwise spatial filters that are
192 not corrupted by zero lag correlations for the dipole pair under consideration. A beamformer
193 with two dipoles in its spatial passband has an identity gain constraint:

$$\mathbf{W}^T \mathbf{H} = \begin{bmatrix} \mathbf{w}_1^T \\ \mathbf{w}_2^T \end{bmatrix} [\mathbf{h}_1 \mathbf{h}_2] = \begin{bmatrix} g_{11} & g_{12} \\ g_{21} & g_{22} \end{bmatrix} = \begin{bmatrix} 1 & 0 \\ 0 & 1 \end{bmatrix} . \quad (7)$$

194 As a consequence, the equation that expresses the estimated pairwise dipolar cross-spectral
195 density reduces to the below equation, in analogy of the model formulation as used in the
196 previous section:

$$\hat{\mathbf{s}}_1 \hat{\mathbf{s}}_2^H = \mathbf{s}_1 \mathbf{s}_2^H + \mathbf{s}_1 \mathbf{N}^H \mathbf{w}_2 + \mathbf{w}_1^T \mathbf{N} \mathbf{s}_2^H + \mathbf{w}_1^T \mathbf{N} \mathbf{N}^H \mathbf{w}_2 . \quad (8)$$

197 Under the assumptions that the cross terms between the noise (*i.e.*, the part of the measured

198 signal that does not originate from the locations of interest) and the considered sources is
199 negligible, and if the noise covariance is assumed spatially white (a scaled identity matrix),
200 then the above equation reduces to:

$$\hat{\mathbf{s}}_1 \hat{\mathbf{s}}_2^H = \mathbf{s}_1 \mathbf{s}_2^H + \sigma \mathbf{w}_1^\top \mathbf{w}_2, \quad (9)$$

201 where σ is a scalar parameter. Under the described (yet most likely often violated) assump-
202 tions, if the true interaction strength between the two dipoles is zero, $\mathbf{s}_1 \mathbf{s}_2^H$ in eq. 9 will be
203 zero. Thus, the estimated cross-spectral density between the two sources may be approximated
204 with a scaled version of the spatial filters' inner product, $\sigma \mathbf{w}_1^\top \mathbf{w}_2$, where the scaling parameter
205 is a function of the pair of source locations. From this follows, that the scaled spatial filter
206 inner product can be used as an approximation of the bias in estimated connectivity under
207 the assumption of no interaction between the considered sources. Pragmatically, we propose
208 to assume the scaling parameter to be fixed for a given seed dipole (*i.e.*, keeping one of the
209 dipoles in the pair fixed, and scanning through the dipole grid for the other dipole of the pair),
210 and thus allow for its estimation by fitting a regression line through a two-dimensional point
211 cloud, which reflects on one dimension the estimated cross-spectral density between the seed
212 dipole and all other dipoles, and on the other dimension the inner product between the seed
213 dipole's spatial filter and the other dipoles' spatial filters. Repeating this fitting procedure for
214 all dipoles and normalizing by the product of the estimated power yields a 6-dimensional vol-
215 ume of null-coherence estimates, which can be used to subtract from the estimated coherence
216 (*cf.* Fig. 1B). The resulting 6-dimensional differential map can subsequently be post-processed
217 (*e.g.*, thresholded) and inspected for local maxima, which might be indicative of truly interact-
218 ing dipoles.

219 **Array subsampling** As will become clear below, these difference maps may still be spatially
220 noisy, resulting in false positive connections (*i.e.*, local maxima that do not reflect interacting
221 dipoles), and true connections being missed (*i.e.*, reconstructed connectivity between locations
222 close to interacting dipoles not presenting as local maxima). To further reduce the spatial
223 noise in the images, we propose a sensor array subsampling approach (Schoffelen et al., 2012;
224 Westner et al., 2015; Westner, 2017). We estimate the 6-dimensional differential connectivity

225 map multiple times, each time using a different random subset between 50 and 150 sensors for
226 the reconstruction (*cf.* Fig. 1C). Although the reconstructions with fewer sensors may have a
227 compromised spatial resolution, the spatial noise will be variable across reconstructions and
228 thus average out, while the true interactions will show up more consistently. This scheme is
229 akin to the idea of Ensemble Methods in machine learning, where the aggregation of many
230 weak learners leads to a strong model with reduced variance (Breiman, 1996).

231 **2 Methods**

232 All simulations and reconstructions were performed in MATLAB (version 2021b) on a Linux
233 operated High Performance Compute cluster, using FieldTrip (Oostenveld et al., 2011) and
234 custom written code.

235 **2.1 MEG sensor data simulations**

236 MEG sensor space complex-valued data matrices were simulated from source space activity,
237 based on a 275-channel axial gradiometer CTF system, as a combination of an ‘ideal’ sensor-
238 level signal data matrix \mathbf{X}_s and a noise data matrix \mathbf{X}_n . These $N_{\text{sensor}} \times N_{\text{observation}}$ matrices
239 reflect the Fourier coefficients (*i.e.*, amplitude and phase information) computed for a given
240 frequency. For the noise matrix we used a multitaper spectral estimate of a frequency band
241 centered around 10 Hz from a 50 second empty room measurement, recorded at the Donders
242 Centre for Cognitive Neuroimaging. The empty room data were segmented into 1 second
243 epochs and spectrally transformed, using a multitaper smoothing parameter of ± 4 Hz (7
244 tapers per segment), which resulted in a 268×350 noise matrix. The number 268 reflects the
245 number of active SQUIDs at the time of the empty room measurement, 350 the number of
246 observations ($N_{\text{epochs}} \times N_{\text{tapers}}$). The signal data matrix was constructed using the generative
247 model $\mathbf{X}_s = \mathbf{HS}$, using a precomputed forward model \mathbf{H} (see below), and an $N_{\text{source}} \times N_{\text{observation}}$
248 matrix \mathbf{S} . The source signals were simulated using MATLAB’s `mvnrnd` function, generating
249 multivariate Gaussian data, with a mean of 0, and a parametrized covariance (cross-spectral
250 density) matrix, defined as:

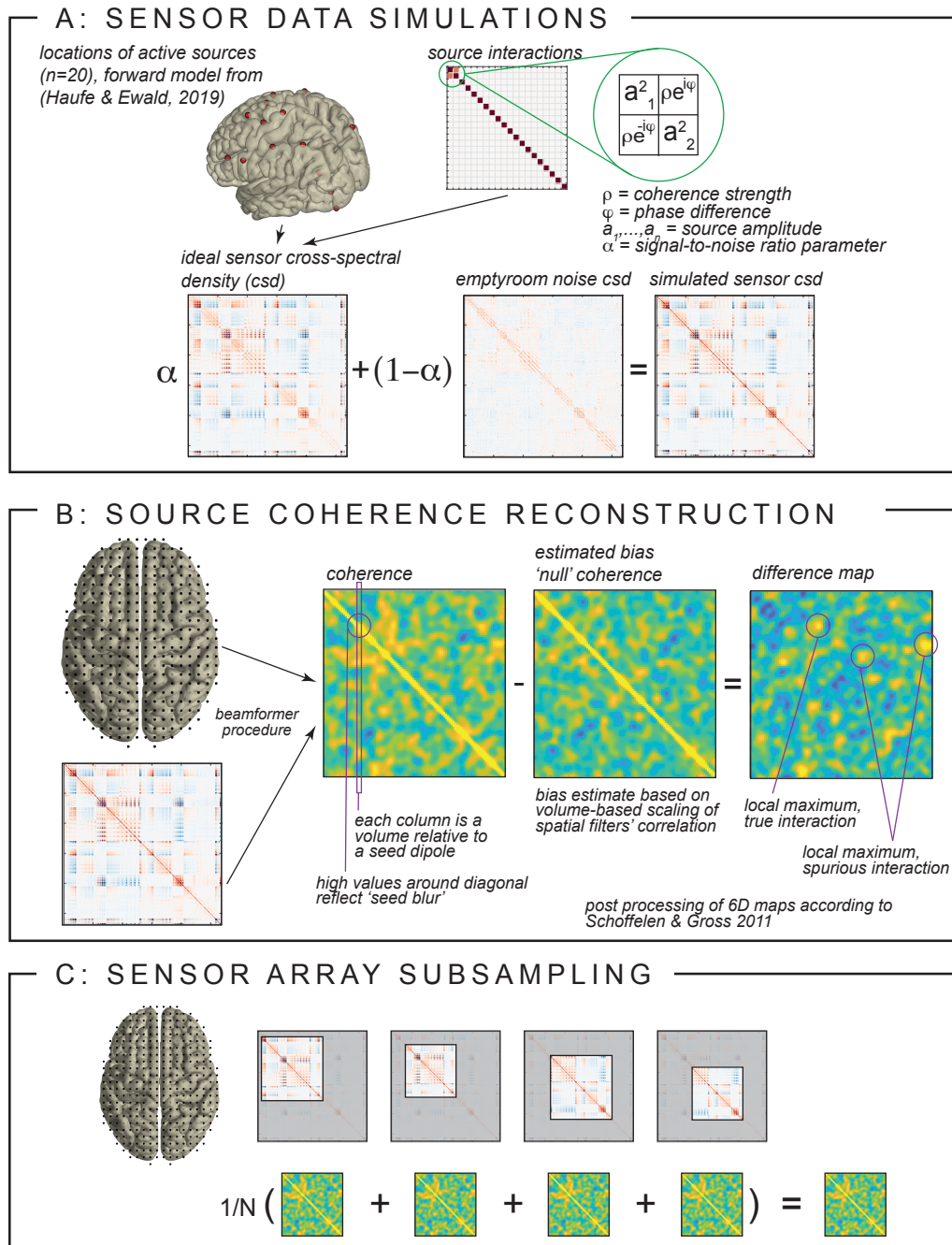


Figure 1: **Simulation and algorithm details.** **A** Setup of sensor data simulation, illustrating the interacting and non-interacting sources and signal-to-noise ratio. **B** Estimation of the null coherence across space and the computation of the difference maps. **C** Illustration of the sensor array subsampling procedure with a varying number of sensors among realizations.

$$\text{diag}(a, a, (1-a), \dots, (1-a)) \begin{bmatrix} 1 & \rho e^{i\varphi} & 0 & \dots & 0 \\ \rho e^{-i\varphi} & 1 & 0 & \dots & 0 \\ 0 & 0 & 1 & \dots & 0 \\ \vdots & \vdots & \vdots & \ddots & \vdots \\ 0 & 0 & 0 & \dots & 1 \end{bmatrix} \text{diag}(a, a, (1-a), \dots, (1-a)) , \quad (10)$$

251 where ρ reflects the intended coherence coefficient between the first 2 sources and φ re-
 252 flects the phase difference. a reflects a relative amplitude parameter, determining the rela-
 253 tive amplitude of the connected dipoles in relation to the other active sources such that the
 254 relative strength between connected dipoles and active sources can be computed as $a/(1 -$
 255 $a)$, *i.e.*, a relative amplitude of 0.8 yields the connected dipoles being four times stronger
 256 than the other active sources. The procedure for simulating the sensor space data is illus-
 257 trated in Figure 1A. For gain matrix \mathbf{H} , we used a precomputed forward model, as described
 258 in [Haufe and Ewald \(2019\)](#) and the Biomag conference 2016 data analysis challenge (see
 259 <https://bbci.de/supplementary/EEGconnectivity/BBCB.html>). Briefly, source locations
 260 were sampled from a cortical segmentation based triangulated mesh, originally consisting of
 261 2004 positions. A three-shell boundary element method (BEM) had been used to compute the
 262 forward solution for the 2004 dipoles with an orientation perpendicular to the cortical sheet,
 263 using Brainstorm ([Tadel et al., 2011](#)). For the simulations presented here, sets of 20 positions
 264 were randomly selected from a subset of 820 positions. This subset was created based on the
 265 norm of the gain vectors for the orientation-constrained dipoles placed at those positions: We
 266 excluded candidate locations for which the sensor array was relatively insensitive, *e.g.*, deep
 267 dipoles in the midline, or dipoles with an unfavorable orientation. The matrices \mathbf{X}_n and \mathbf{X}_s
 268 were scaled with the Frobenius norm of their respective cross-spectral densities ($\mathbf{X}\mathbf{X}^H$) and
 269 linearly combined using:

$$\mathbf{X} = \sigma \mathbf{X}_s + (1 - \sigma) \mathbf{X}_n , \quad (11)$$

270 where σ is a parameter that determines the signal-to-noise ratio. Table 1 summarizes the rel-
 271 evant parameters for the simulations and the values used to explore the different reconstruction

272 approaches.

parameter	values
# of active sources	20 in 100 different configurations
σ , signal-to-sensor-noise	0.5*, 0.6
a , amplitude relation	0.5*, 0.7, 0.8*
ρ , coherence coefficient	0, 0.2, 0.3, 0.4, 0.5, 0.6, 0.7, 0.8
π , phase difference	0, $(2/17)\pi$, $(4/17)\pi$, $(8/17)\pi$, $(16/17)\pi$

Table 1: **Simulation parameters.** Values marked with asterisks denote values for which the outcomes are reported in the supplementary material.

273 2.2 Beamformer source reconstruction and coherence estimation

274 For source reconstruction we used a forward model defined on a regularly spaced 3-dimensional
275 dipole grid (with a spacing of 8 mm). The brain compartment of this grid consisted of 4416
276 dipoles and was defined by the same anatomical MRI as the one used for the simulations' forward
277 model. For the reconstructions' forward model, we used a single shell model as implemented
278 in FieldTrip (Nolte, 2003). Our detailed analysis required the computation of 4416^2 pairs
279 of spatial filters for many iterations of sensor array subsamples (we used 100 subsamples per
280 simulation) over 8000 parameter combinations. Thus, we had to estimate over 15 trillion spatial
281 filters in total. We wrote custom code for the efficient computation of the spatial filters and
282 the derived coherence. All beamformers were computed with FieldTrip's `fixedori` constraint,
283 which computes a fixed orientation forward model for each dipole, based on the maximization
284 of the beamformer's output power (Sekihara and Nagarajan, 2008).

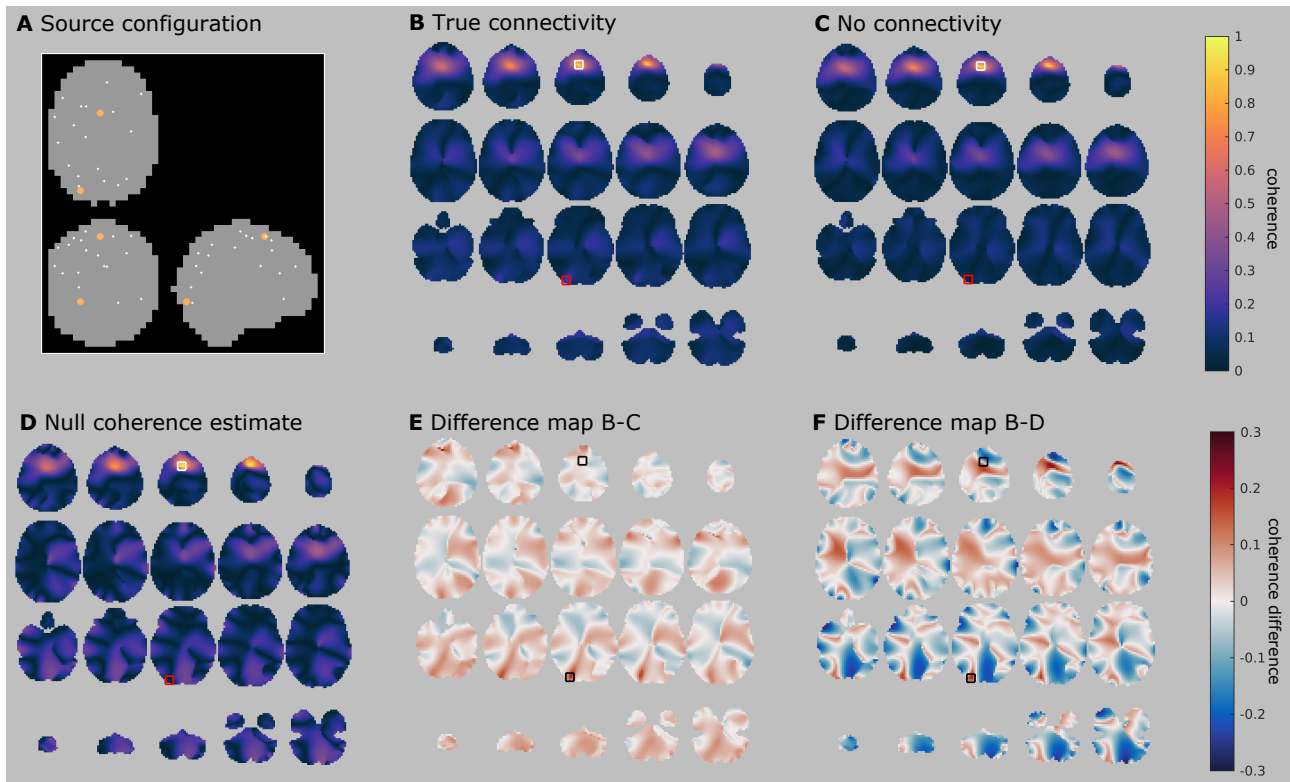
285 3 Results

286 3.1 Illustrative example and null coherence estimation

287 This section illustrates our proposed approach. Figure 2A shows the spatial configuration of
288 one instantiation of the simulation, where 20 dipole locations were randomly selected to reflect
289 the active sources. Two of these sources (the bigger, orange dots in the figure, here denoted as a
290 medial superior frontal (MSF) and left occipital (LO) source) reflect the interacting dipoles. To
291 illustrate the potential issues related to spatial leakage, we start by investigating different seed-

292 based maps. In this example, we simulated the interaction to be at a phase difference of $(8/17)\pi$
293 and the coherence strength to be 0.5. For illustration purposes we computed these seed-based
294 results on a 4 mm grid, but for the reconstruction of all pairwise interactions we used an 8
295 mm grid. For this example, we also simulated data using identical source parameters as for the
296 above simulations, apart from the coherence strength, which was set to zero. This simulation
297 was intended to reflect a perfect baseline, where everything except the interaction strength
298 was kept constant. We start the illustration using a traditional single dipole beamformer.
299 Figure 2B shows the seed-based estimate of coherence for truly interacting sources, using as
300 a seed the grid position that was closest to the MSF source (indicated with a white square).
301 Figure 2C shows an estimate of the coherence for the scenario in which the dipoles were not
302 connected. Both estimates are dominated by the well-known seed blur, but also show a small
303 local maximum in the vicinity of the LO source (indicated with a red square) for the case of
304 the true connectivity (Fig. 2B). The difference image (Fig. 2E) shows an effective suppression
305 of the leakage close to the seed location. Yet, there is considerable spatial structure in the
306 residual image, and although there is a local maximum in the vicinity of the LO source, there
307 are also other maxima in this image that may be mistaken for interacting sources. In many
308 practical situations, an appropriate baseline condition is not available. This motivated us to
309 estimate the ‘null’ coherence based on the scaled inner product of the spatial filters (as described
310 above), assuming this scaling to be fixed for a given seed dipole, and the noise to be spatially
311 white and uncorrelated with the sources. Figure 2D shows the computed null coherence for
312 our illustrative example. The null coherence map shows considerably more structure than the
313 baseline condition in Figure 2C, and thus, the difference map between the coherence and null
314 coherence (Fig. 2F) also exhibits more substantial structure than the difference map with the
315 baseline condition (Fig. 2E). Specifically, the seed blur does not seem to be very well accounted
316 for given the difference map’s local maximum in the vicinity of the MSF seed region. However,
317 the local maximum in the vicinity of the LO source is more prominent in this figure than in
318 Figure 2E.

319 Before exploring the usage of different beamformer analysis schemes to improve the connec-
320 tivity results from Figure 2, let us note that Figure 2 considered a situation in which the seed
321 dipole for the connectivity estimation was well chosen, *i.e.*, it coincided roughly with one of the



322 truly interacting sources. In the analysis of experimental data, seed locations are not known a
323 priori, thus one might happen to choose locations that are not truly interacting. In this case,
324 the high spatial structure in the null coherence maps is replicated even for non-interacting
325 seeds, which evidently would be problematic for real data analysis. This effect is illustrated in
326 supplementary Figure S1.

327 **3.2 Two-dipole beamformer and array subsampling**

328 At this point, one may argue that the suggested null coherence estimate is impractical to use,
329 given the large amount of residual noise in the difference images (*cf.* Figures 1 and S1). In
330 other words, the spurious connectivity estimated between two locations is poorly approximated
331 just by computing the spatial leakage of projected spatially white sensor noise, at least when
332 using a single dipole beamformer formulation. As motivated in the introduction section, the
333 use of a two dipole-constraint in the beamformer formulation may reduce some of the leakage
334 terms in equation 6, leading to a null coherence estimate that is better behaved. In addition,
335 sensor array subsampling allows for multiple (although possibly degraded) estimates of the
336 true structure in the data, while unstructured noise is averaged out when aggregating those
337 estimates. Let us further investigate if the scaled spatial filter inner product might be an
338 appropriate estimate for spurious source interactions when using those alternative beamformer
339 approaches. Figure 3A revisits the results from Figure 2F, plotting the estimated null coherence
340 (x-axis) against the estimated coherence (y-axis) for all dipoles in the stimulation with the values
341 for the interacting dipole pair highlighted with the yellow square. Figure 3B and C show the
342 results for the same single dipole beamformer approach but with the other truly interacting
343 source and a source between the two truly interacting sources as seeds, respectively. Ideally,
344 for non-interacting dipoles, the data points should cluster on a line around the diagonal, while
345 the data point(s) corresponding to the truly interacting dipoles should be clearly above the
346 diagonal. Comparing the single dipole beamformer (Figure 3A and B) with the two-dipole
347 beamformer (Figure 3D and E) for the truly interacting dipoles suggests that, overall, the
348 data points cluster more nicely around the diagonal line in the two-dipole beamformer case.
349 Figure 3G-I depict the results of the subsampling approach. To this end, the average across
350 subsamples of the estimated coherence and null coherence was normalized with the standard

351 deviation of their difference. Here, the subsampling boosts the detectability of the interacting
352 dipole pair, by making it stand out clearly from all other dipole pairs. Also, for seed dipoles in
353 inactive and non-interacting locations (bottom row), the spread of the data points around the
354 diagonal is much more comparable across the different seed dipoles for the subsampling-based
355 reconstruction. In contrast, when no subsampling is used, the deviations from the diagonal
356 are substantially larger for the inactive seed dipole as compared to the active and interacting
357 seed dipoles. This suggests that the magnitude of the spatial noise in the difference images
358 varies considerably, depending on the choice of the seed dipole, and that the approach of array
359 subsampling mitigates this effect by aggregating the results of many different noise realizations.

360 **3.3 Evaluating all-to-all pairwise coherence**

361 To formally evaluate how the spurious spatial structure in the seed-based connectivity maps
362 interacts with accurate detectability of the true interactions, we constructed and evaluated the
363 all-to-all pairwise coherence matrix (Schoffelen and Gross, 2011). Here, each of the dipoles in
364 the grid serves as a seed dipole to all other dipoles. After the subtraction of an estimate of
365 the null coherence, the resulting 6-dimensional volume of difference in coherence is thresholded,
366 using a relative threshold keeping the $N\%$ largest values. We explored the following values of N ,
367 with the corresponding number of unique supra threshold edges in parentheses: 5% (9.8×10^5),
368 1% (1.95×10^5), 0.5% (9.8×10^4), 0.1% (1.95×10^4), 0.05% (9.8×10^3), 0.01% (1.95×10^3),
369 0.005% (975), 0.001% (195), 0.0005% (98).

370 The thresholded maps are subsequently analyzed for the presence of clusters of spatially
371 connected dipoles in 6-dimensional space. Such clusters are considered to reflect a potential
372 long-distance interaction if they consist of two dipole assemblies that are spatially distinct
373 from each other. Clusters that contain auto-connections, *i.e.*, dipoles that are present in both
374 assemblies of the connection, are discarded from further inspection. If the simulated interacting
375 dipoles fall within the identified clusters, it is considered a hit. All remaining clusters are
376 considered false positives. It should be noted that the number of false positives evidently will
377 increase with a decreasing threshold when using a relative thresholding scheme as we do here.
378 The total number of false positives further depends on the blurriness of the spatial noise and
379 the degree of auto-connectedness in the data.

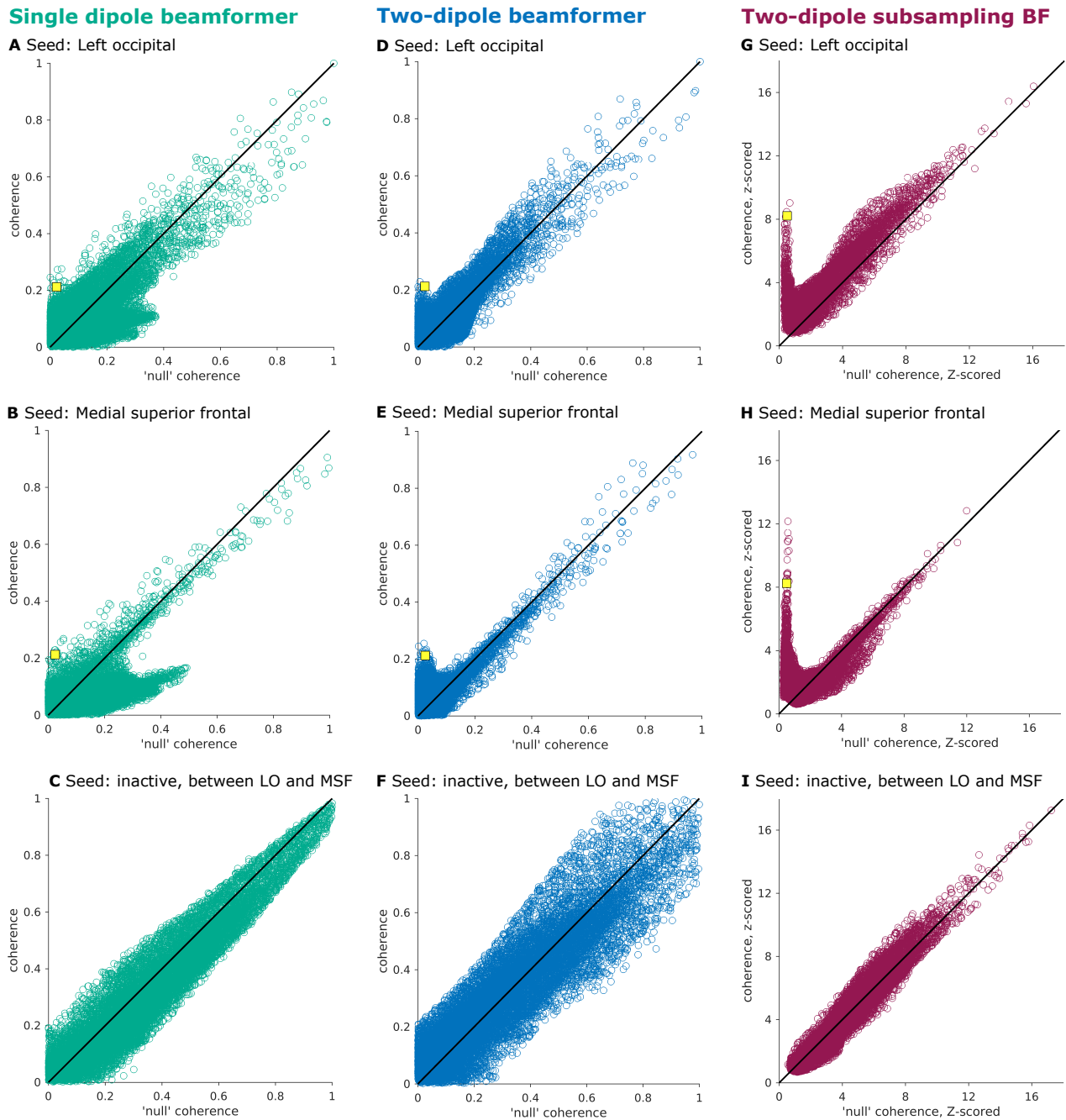


Figure 3: **Comparing different beamformer approaches.** **A-C** Single dipole beamformer with **A** seed close to truly interacting source in left occipital cortex (LO), **B** seed close to truly interacting source in medial superior frontal cortex (MSF), and **C** seed in a non-active dipole located on the line between interacting dipoles LO and MSF. **D-F** Two-dipole beamformer. **G-I** Two-dipole beamformer with array subsampling. The values for the interacting dipole pair highlighted with the yellow square.

380 Figure 4 shows the clusters with the smallest distance to the simulated interacting dipole
381 pair, and the number of distinct connections, for each of the different thresholds applied. Using
382 a single dipole beamformer (Fig. 4A), the true connection can be correctly identified in three
383 out of the nine thresholding schemes (marked with a red frame). This, however, comes at the
384 expense of additional false positive connections, ranging in number from 70 to 128. Thus, in
385 this relatively favorable context – where coherence is large and the phase of the interaction is
386 close to 90 degrees, *i.e.*, with only a minor instantaneous correlation between the two sources
387 without the potential corresponding distortion of the beamformer due to correlated sources –
388 the actual connection may be correctly identified, but one has to be prepared to accept an
389 additional large number of false positives.

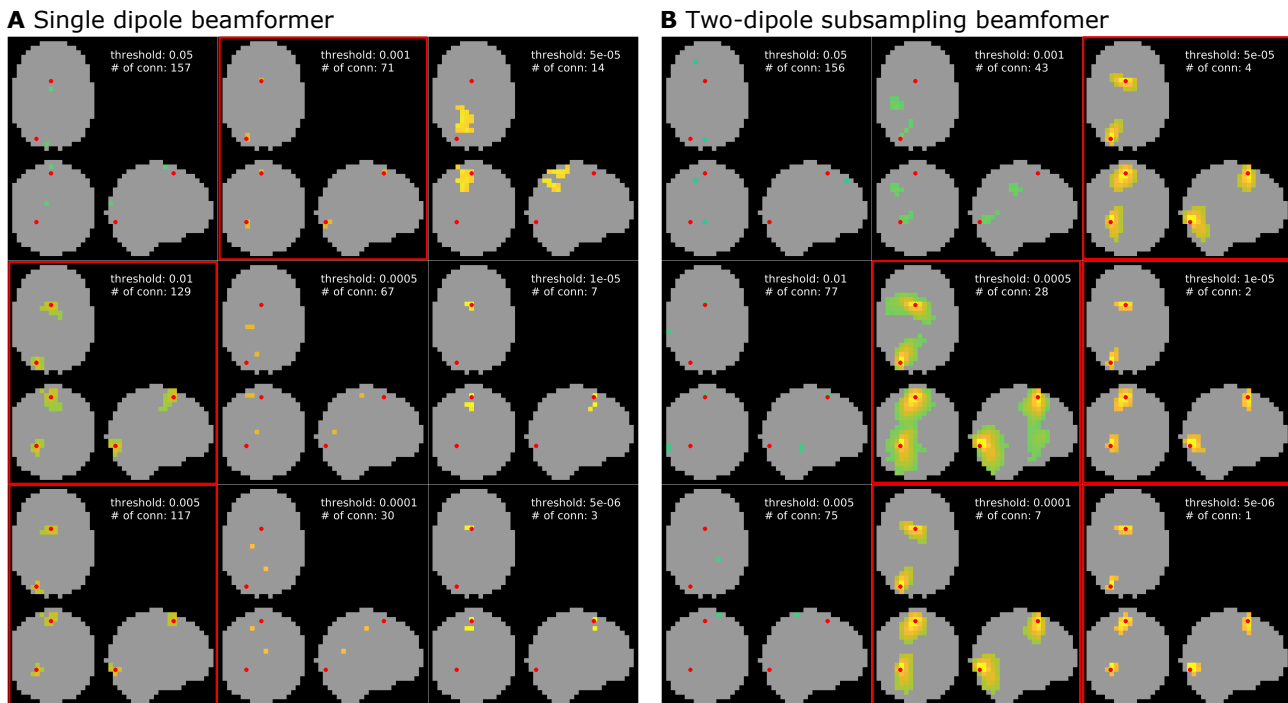


Figure 4: **All-to-all pairwise coherence.** Shown are the results at different cluster thresholds for the single dipole beamformer (A) and the two-dipole beamformer with array subsampling (B). Each result also lists the number of identified connections. Thresholds at which the truly interacting dipole pair was successfully identified are marked by a red frame.

390 Figure 4B shows the spatial clusters closest to the interacting dipole pair for the subsampling-
391 based reconstruction. Here, the interacting sources are correctly identified in the five highest
392 thresholding schemes (marked with red frames), with a considerable reduction in the number of
393 false positives as compared to the single dipole beamformer output in Figure 4A. The number
394 of false positives drops to one or none for the highest two thresholds applied. As an alternative
395 to analyzing the difference in coherence with an approximation of the estimated bias under the

396 assumption of no coherence, one can also investigate the magnitude of the imaginary part of
397 the reconstructed coherency. Figure S2 in the supplementary material replicates the results
398 from Figure 2A (using a single dipole beamformer) for the imaginary part of coherency. With
399 increasing threshold, the true connection can still be reliably identified and the number of false
400 positives drops to only two for the highest two thresholds tested. Importantly, however, the
401 usefulness of the imaginary part of coherency is limited to situations in which the phase dif-
402 ference of the interaction is pointing away from 0 or 180 degrees. Figure 5 shows the results
403 for the same interacting dipole pair as in all previous examples, which are now interacting at a
404 phase difference of zero. The subsampling approach (Fig. 5B) is still capable of detecting the
405 interacting dipole pair at high thresholds, whereas the imaginary part of coherency approach
406 (Fig. 5A) now fails at higher thresholds. Therefore, the subsampling approach with a two-dipole
407 beamformer seems to work well regardless of the phase difference of the interacting dipole pair.

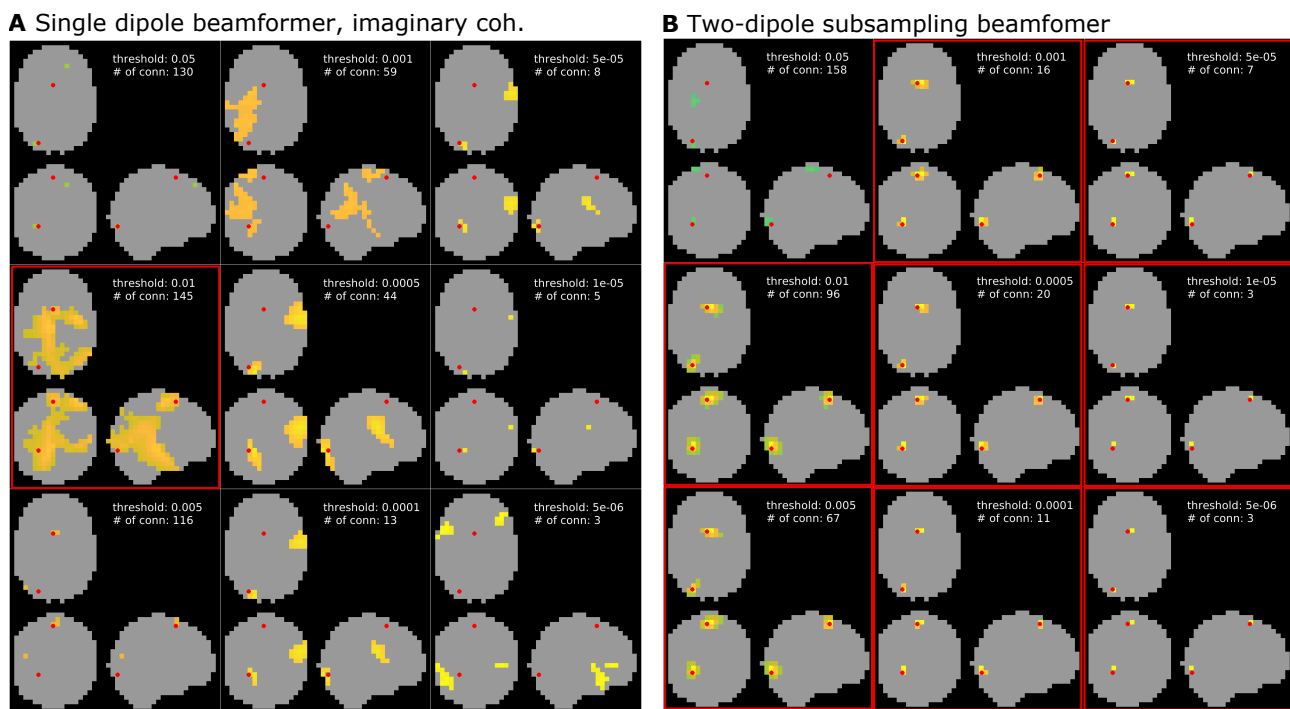


Figure 5: **Impact of 0 degree phase shift.** Results for interacting sources where the phase of the interaction is 0 degrees for the beamformer with the geometric correction scheme, which focuses on the imaginary part of coherency (A) and the two-dipole beamformer with array subsampling (B). Each result also lists the number of identified connections. Thresholds at which the truly interacting dipole pair was successfully identified are marked by a red frame.

408 3.4 Full simulation results

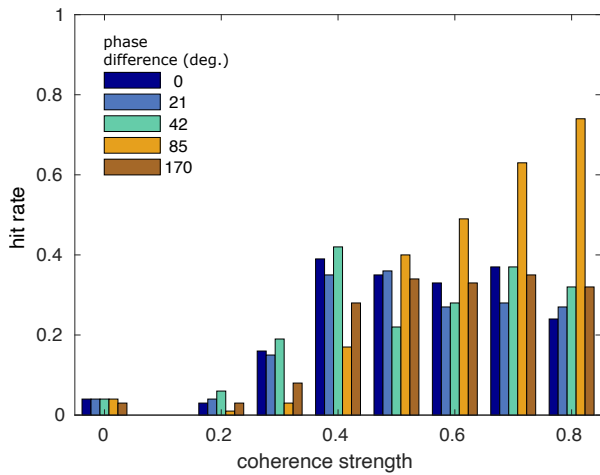
409 To test our proposed approach more thoroughly and to substantiate the illustrative results
410 discussed so far, we employed an exhaustive simulation. Here, we compare the array subsam-
411 pling two-dipole beamformer approach to three other approaches: the traditional single dipole
412 beamformer, the two-dipole beamformer without subsampling, and a beamformer without sub-
413 sampling, using a geometric correction scheme, proposed by [Wens et al. \(2015\)](#). This correction
414 scheme uses a spatial projection heuristic to remove instantaneous leakage from a seed location's
415 estimated activity from all target locations' estimated activity. In practice, this results in the
416 real-valued component of the interaction between the seed and target dipoles to be suppressed,
417 leading to a purely imaginary-valued coherency value. Therefore, in the below, we refer to this
418 last strategy as the reconstruction of the imaginary part of coherency. We evaluate the source
419 reconstruction results based on hit rate, *i.e.*, how often the chosen approach correctly identified
420 the true interacting dipole pair. Fig. 6 shows the simulation results for a relative amplitude of
421 $a = 0.7$, thus, the interacting sources were 2.333 times stronger than the other active sources
422 (for the results for $a = 0.5$ and $a = 0.8$, we refer the reader to supplementary Figures S3 and
423 S4, respectively). The results reported in the paper are based on a signal-to-sensor-noise ratio
424 of 0.6, the results for an SNR of 0.5 are reported in supplementary Figures S6-S8.

425 Fig. 6 depicts the hit rate as a function of simulated coherence strength, and phase difference,
426 for the different reconstruction strategies. We first considered the situation in which application
427 of at least one of the thresholds $< 0.01\%$ resulted in the detection of the dipole pair that was
428 chosen for the interaction (to define a hit, we allowed the summed distance of the simulated
429 dipoles to the closest voxel in the suprathreshold clusters to be at most 2 cm). Overall, the
430 performance of the single dipole approach (Fig. 6A) was quite poor, with the hit rate —
431 as a function of coherence strength and phase difference — rarely exceeding 40%. Only at
432 unrealistically high coherence strengths > 0.6 was the detection rate larger than 50%, and even
433 then only at phase differences close to 90 degrees. The two-dipole approach (Fig. 6B) fared
434 better, specifically for coherence values larger than 0.4. The single dipole beamformer using
435 imaginary coherency (Fig. 6C) generally showed better performance, already at lower coherence
436 values, but this performance was highly dependent on the phase difference of the interaction,
437 where interactions with a phase difference close to 90 degrees were more readily detectable,

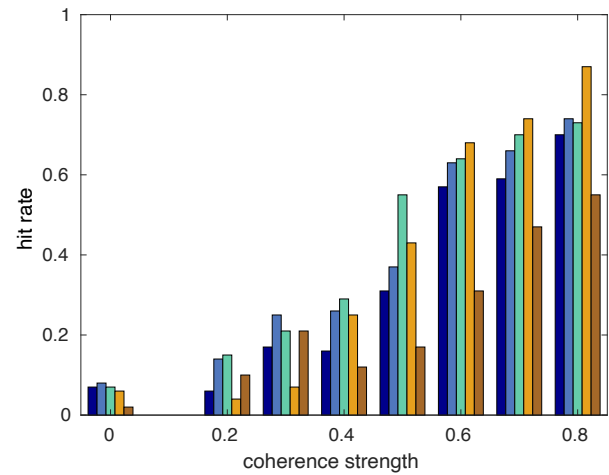
438 reaching a hit rate of $> 90\%$ in some situations. When the phase difference of the interaction
439 was close to 0 (or 180) degrees, however, the detection rate at higher coherence values was
440 only slightly higher than for low coherence strengths, compared with the single and two-dipole
441 approach. The array subsampling beamformer (Fig. 6D) overall performed best. Even though
442 the maximum detection rate was not as high as in some situations using the imaginary part of
443 coherency (*i.e.*, coherence > 0.5 and phase difference close to 90 degrees), the detection rate at
444 a moderate coherence of 0.3 already exceeded 60%, independent of the phase difference. Thus,
445 the array subsampling two-dipole beamformer outperforms the other approaches for almost all
446 parameters, specifically considering the fact that physiologically realistic neuronal interactions
447 are not constrained to phase differences close to 90 degrees, nor are those interactions restricted
448 to high coherence values. The findings depicted in Fig. 6 are at large supported by the results
449 of other amplitude and SNR values, as supplementary Figures S4 and S6-S8 illustrate.

450 Notably, in the absence of simulated true coherence, the different reconstruction approaches
451 resulted in a variable amount of false positive connections in the direct vicinity of a pair of ac-
452 tivated dipoles (see the leftmost set of bars in each of the panels in Fig. 6). For the imaginary
453 part of coherency this type of false positive connection was present in about 30% of the sim-
454 ulations, and for the proposed subsampling approach the percentage of occurrence was about
455 10%. In general, the occurrence of false positives is the consequence of the fact that we used a
456 relative thresholding scheme to investigate the spatial structure of the reconstructed connectiv-
457 ity maps. By construction, and irrespective of the numeric value of the connectivity estimates,
458 the relative thresholding scheme always results in a collection of suprathreshold edges in the
459 connectivity maps, which may be spatially clustered, and interpreted as interacting sources.
460 Based on the spatial smoothness of the connectivity maps, and the number of suprathreshold
461 edges, the number of false positive connections will vary as a function of the chosen thresh-
462 old. Fig. 7 shows the number of false positives versus the hit rate in a so-called Free-response
463 Receiver-Operating-Characteristic (FROC), as a function of the detection threshold and for a
464 relative amplitude of $a = 0.7$. On each of the lines, the threshold is increasing from left to
465 right. For all but the subsampling reconstruction method, the optimal — yet still quite low
466 — sensitivity was reached at a threshold that yielded close to 100 false positive connections on
467 average. For the subsampling reconstruction method, the highest sensitivity was compromised

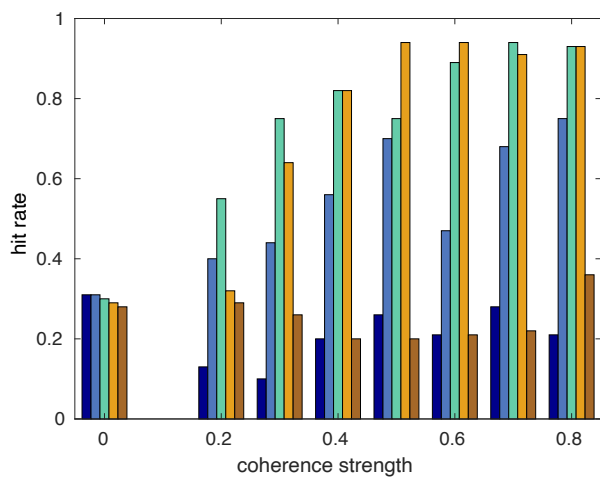
A Single dipole beamformer, coherence



B Two-dipole beamformer, coherence



C Single dipole beamformer, imag. coh.



D Two-dipole subsampling BF, coherence

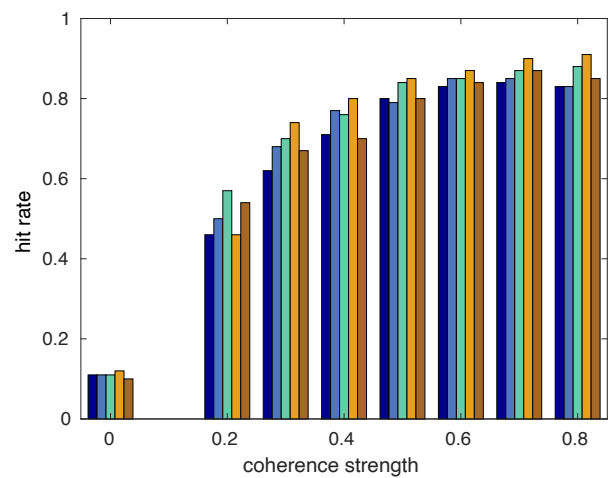


Figure 6: **Detection rate for interacting dipole pairs.** Results from the full simulation, showing the hit rates for the interacting dipole pair as a function of simulated coherence strength and phase difference. The relative amplitude of the interacting sources and the other sources was $a = 0.7$, *i.e.*, the interacting sources were 2.333 times stronger than the other active sources. The SNR was 0.6. **A** Traditional single dipole beamformer. **B** Two-dipole beamformer. **C** Single dipole beamformer using imaginary coherence. **D** Two-dipole beamformer with array subsampling.

468 by about 10 to 20 false positive connections on average. Although this still may seem a rather
469 high false positive rate, it is substantially lower than the false positive rate for the other ap-
470 proaches tested. The FROC curves for relative amplitudes of $a = 0.5$ and $a = 0.8$ can be found
471 in the supplementary material (Fig. S5) and show very similar patterns. For an SNR of 0.5, the
472 results are reported in supplementary Figure S9 and at large support the findings for an SNR of
473 0.6, except for at a low relative amplitude of $a = 0.5$, the only parameter combination for which
474 the two-dipole subsampling beamformer does not clearly outperform the other algorithms.

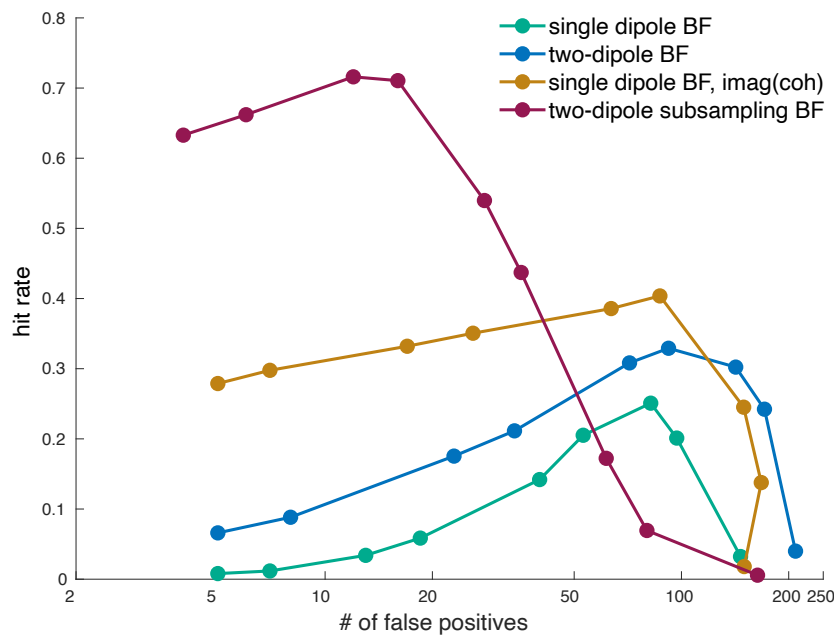


Figure 7: **Free-response Receiver-Operating-Characteristic.** Hit rate plotted against the number of false positive connections at a relative amplitude of $a = 0.7$.

475 4 Discussion and future directions

476 Brain connectivity plays a central role in many prevalent hypotheses on brain functioning and
477 organization (Fries, 2005; Jensen and Mazaheri, 2010; Fries, 2015; Bonnefond et al., 2017).
478 Thus, the estimation of functional connectivity based on electrophysiological processes is a
479 necessary tool for the experimental assessment of those theories. Over the years, many different
480 measures of brain connectivity have been put forward (Aviyente et al., 2011; Vinck et al., 2011;
481 Ghanbari and Moradi, 2020) and the methods to apply these have been refined (Dalal et al.,
482 2006; Kuznetsova et al., 2021; Woolrich et al., 2011; Hillebrand et al., 2012; Nunes et al., 2020).

483 Despite these efforts, results from non-invasive recordings, especially phase synchrony measures,
484 have stayed sparse and methodological challenges remain (Colclough et al., 2016; Bastos and
485 Schoffelen, 2016; Palva et al., 2018; He et al., 2019; Schoffelen and Gross, 2009). In this paper,
486 we aimed at addressing some of these challenges through a new beamformer-based connectivity
487 estimation framework, which utilizes three key components: a two-dipole beamformer approach
488 to estimate all-to-all connectivity, an estimation of the null coherence of the model under the
489 assumption of no interaction, and a sensor array subsampling approach to further mitigate the
490 influence of spatial noise. Our all-to-all approach is motivated by the fact that — even in an
491 unrealistically well-controlled contrast — misspecification of the seed dipoles leads to spatial
492 structure in connectivity difference maps that can be mistaken for true interactions. Moreover,
493 because experimental contrasts almost invariably contain differences in source activations and
494 SNR, difference maps of connectivity may show spatial structure that is not due to changes in
495 actual interaction between sources. For this reason, it is desirable to estimate the spatial leakage
496 of connectivity directly from the data. We explored the possibility to use such null coherence
497 estimates, based on the weighted inner product between pairs of spatial filters. A two-dipole
498 beamformer model is motivated by the notion that beamformer estimates are distorted in the
499 presence of underlying correlations. Furthermore, we propose to use sensor array subsampling
500 in order to smooth out the spatial noise at the benefit of the true interactions.

501 Some of the key components of our approach have been proposed before, in one form or
502 another, but mostly with a different intention, and were never combined for the assessment of
503 connectivity. We compared the performance of our approach to other all-to-all reconstruction
504 schemes, which used only a subset — or none — of the key components.

505 Using an extensive set of simulations we showed that our approach outperforms the other,
506 often more traditional, all-to-all approaches tested. The overall detection rate, specifically
507 at physiologically meaningful interaction strengths and at a wide range of phase angles, was
508 highest for the proposed subsampling based method. This high detection rate was accompanied
509 by the overall lowest false positive rate. While performance was considerably affected when the
510 relative source amplitude of competing, non-interacting sources was increased (supplementary
511 Figure S3), our approach still showed the overall lowest false positive rate (Figure S5A). Based
512 on these observations, we argue that the proposed reconstruction approach can be a promising

513 pipeline to be evaluated on real MEG data for the robust detection of phase synchronization
514 in brain networks.

515 Apart from the evaluation of the utility of the proposed approach on real experimental
516 data, we foresee future work to explore in more detail certain aspects of the proposed analysis
517 scheme. For instance, regarding the subsampling, we have settled on a fixed number of subsam-
518 pled reconstructions, using a random number of sensors (between 50 and 150), and combined
519 the reconstructions by means of averaging. Although those parameter choices were motivated
520 by initial explorations, strategies to estimate the optimal number of sensors for the subsam-
521 pling, and different combinatorial strategies (*e.g.*, by also taking the variance structure across
522 subsample based reconstructions into account) may further improve the performance of the
523 subsampling based approach.

Acknowledgments

This work was supported by the European Union’s Horizon 2020 Marie Skłodowska Curie Individual Fellowship (grant agreement 893912) to BUW.

References

- Aviyente S, Bernat EM, Evans WS, Sponheim SR (2011) A phase synchrony measure for quantifying dynamic functional integration in the brain. *Human Brain Mapping* 32:80–93.
- Baker AP, Brookes MJ, Rezek IA, Smith SM, Behrens T, Probert Smith PJ, Woolrich M (2014) Fast transient networks in spontaneous human brain activity. *eLife* 3:e01867.
- Bastos AM, Schoffelen JM (2016) A Tutorial Review of Functional Connectivity Analysis Methods and Their Interpretational Pitfalls. *Frontiers in Systems Neuroscience* 9.
- Bonnefond M, Kastner S, Jensen O (2017) Communication between Brain Areas Based on Nested Oscillations. *eneuro* 4:ENEURO.0153–16.2017.
- Breiman L (1996) Bagging predictors. *Machine Learning* 24:123–140.
- Brookes MJ, Stevenson CM, Barnes GR, Hillebrand A, Simpson MI, Francis ST, Morris PG (2007) Beamformer reconstruction of correlated sources using a modified source model. *NeuroImage* 34:1454–1465.
- Brookes MJ, Woolrich M, Luckhoo H, Price D, Hale JR, Stephenson MC, Barnes GR, Smith SM, Morris PG (2011) Investigating the electrophysiological basis of resting state networks using magnetoencephalography. *Proceedings of the National Academy of Sciences* 108:16783–16788.
- Brookes M, Woolrich M, Barnes G (2012) Measuring functional connectivity in MEG: A multivariate approach insensitive to linear source leakage. *NeuroImage* 63:910–920.
- Colclough G, Brookes M, Smith S, Woolrich M (2015) A symmetric multivariate leakage correction for MEG connectomes. *NeuroImage* 117:439–448.
- Colclough G, Woolrich M, Tewarie P, Brookes M, Quinn A, Smith S (2016) How reliable are MEG resting-state connectivity metrics? *NeuroImage* 138:284–293.
- Dalal S, Sekihara K, Nagarajan S (2006) Modified Beamformers for Coherent Source Region Suppression. *IEEE Transactions on Biomedical Engineering* 53:1357–1363.
- de Pasquale F, Della Penna S, Sporns O, Romani GL, Corbetta M (2016) A Dynamic Core Network and Global Efficiency in the Resting Human Brain. *Cerebral Cortex* 26:4015–4033.

- Ewald A, Marzetti L, Zappasodi F, Meinecke FC, Nolte G (2012) Estimating true brain connectivity from EEG/MEG data invariant to linear and static transformations in sensor space. *NeuroImage* 60:476–488.
- Fries P (2005) A mechanism for cognitive dynamics: Neuronal communication through neuronal coherence. *Trends in Cognitive Sciences* 9:474–480.
- Fries P (2015) Rhythms for Cognition: Communication through Coherence. *Neuron* 88:220–235.
- Ghanbari Z, Moradi MH (2020) FSIFT-PLV: An emerging phase synchrony index. *Biomedical Signal Processing and Control* 57:101764.
- Gross J, Kujala J, Hamalainen M, Timmermann L, Schnitzler A, Salmelin R (2001) Dynamic imaging of coherent sources: Studying neural interactions in the human brain. *Proceedings of the National Academy of Sciences* 98:694–699.
- Haufe S, Ewald A (2019) A Simulation Framework for Benchmarking EEG-Based Brain Connectivity Estimation Methodologies. *Brain Topography* 32:625–642.
- He B, Astolfi L, Valdes-Sosa PA, Marinazzo D, Palva SO, Benar CG, Michel CM, Koenig T (2019) Electrophysiological Brain Connectivity: Theory and Implementation. *IEEE Transactions on Biomedical Engineering* 66:2115–2137.
- Hillebrand A, Barnes GR, Bosboom JL, Berendse HW, Stam CJ (2012) Frequency-dependent functional connectivity within resting-state networks: An atlas-based MEG beamformer solution. *NeuroImage* 59:3909–3921.
- Hipp JF, Hawellek DJ, Corbetta M, Siegel M, Engel AK (2012) Large-scale cortical correlation structure of spontaneous oscillatory activity. *Nature Neuroscience* 15:884–890.
- Jensen O, Mazaheri A (2010) Shaping Functional Architecture by Oscillatory Alpha Activity: Gating by Inhibition. *Frontiers in Human Neuroscience* 4.
- Kuznetsova A, Nurislamova Y, Ossadtchi A (2021) Modified covariance beamformer for solving MEG inverse problem in the environment with correlated sources. *NeuroImage* 228:117677.

- Moiseev A, Gaspar JM, Schneider JA, Herdman AT (2011) Application of multi-source minimum variance beamformers for reconstruction of correlated neural activity. *NeuroImage* 58:481–496.
- Nolte G (2003) The magnetic lead field theorem in the quasi-static approximation and its use for magnetoencephalography forward calculation in realistic volume conductors. *Physics in Medicine and Biology* 48:3637–3652.
- Nolte G, Bai O, Wheaton L, Mari Z, Vorbach S, Hallett M (2004) Identifying true brain interaction from EEG data using the imaginary part of coherency. *Clinical Neurophysiology* 115:2292–2307.
- Nunes AS, Moiseev A, Kozhemiako N, Cheung T, Ribary U, Doesburg SM (2020) Multiple constrained minimum variance beamformer (MCMV) performance in connectivity analyses. *NeuroImage* 208:116386.
- O’Neill GC, Tewarie P, Vidaurre D, Liuzzi L, Woolrich MW, Brookes MJ (2018) Dynamics of large-scale electrophysiological networks: A technical review. *NeuroImage* 180:559–576.
- Oostenveld R, Fries P, Maris E, Schoffelen JM (2011) FieldTrip: Open Source Software for Advanced Analysis of MEG, EEG, and Invasive Electrophysiological Data. *Computational Intelligence and Neuroscience* 2011:1–9.
- Palva JM, Wang SH, Palva S, Zhigalov A, Monto S, Brookes MJ, Schoffelen JM, Jerbi K (2018) Ghost interactions in MEG/EEG source space: A note of caution on inter-areal coupling measures. *NeuroImage* 173:632–643.
- Pollok B, Gross J, Dirks M, Timmermann L, Schnitzler A (2004) The cerebral oscillatory network of voluntary tremor: Cerebral oscillatory network of voluntary tremor. *The Journal of Physiology* 554:871–878.
- Pollok B, Gross J, Müller K, Aschersleben G, Schnitzler A (2005) The cerebral oscillatory network associated with auditorily paced finger movements. *NeuroImage* 24:646–655.
- Schoffelen JM, Gross J (2009) Source connectivity analysis with MEG and EEG. *Human Brain Mapping* 30:1857–1865.

- Schoffelen JM, Gross J (2011) Improving the interpretability of all-to-all pairwise source connectivity analysis in MEG with nonhomogeneous smoothing. *Human Brain Mapping* 32:426–437.
- Schoffelen JM, Gross J, Oostenveld R (2012) Improvement of beamformer source reconstruction using sensor-array subsampling In *BIOMAG 2012 - 18th International Conference on Biomagnetism*.
- Schoffelen JM, Oostenveld R, Fries P (2005) Neuronal Coherence as a Mechanism of Effective Corticospinal Interaction. *Science* 308:111–113.
- Schoffelen JM, Oostenveld R, Fries P (2008) Imaging the human motor system’s beta-band synchronization during isometric contraction. *NeuroImage* 41:437–447.
- Sekihara K, Nagarajan SS (2008) *Adaptive Spatial Filters for Electromagnetic Brain Imaging* Series in Biomedical Engineering.
- Tadel F, Baillet S, Mosher JC, Pantazis D, Leahy RM (2011) Brainstorm: A User-Friendly Application for MEG/EEG Analysis. *Computational Intelligence and Neuroscience* 2011:1–13.
- Timmermann L, Gross J, Dirks M, Volkmann J, Freund HJ, Schnitzler A (2003) The cerebral oscillatory network of parkinsonian resting tremor. *Brain* 126:199–212.
- Van Veen B, Van Drongelen W, Yuchtman M, Suzuki A (1997) Localization of brain electrical activity via linearly constrained minimum variance spatial filtering. *IEEE Transactions on Biomedical Engineering* 44:867–880.
- Varela F, Lachaux JP, Rodriguez E, Martinerie J (2001) The brainweb: Phase synchronization and large-scale integration. *Nature Reviews Neuroscience* 2:229–239.
- Vinck M, Oostenveld R, van Wingerden M, Battaglia F, Pennartz CM (2011) An improved index of phase-synchronization for electrophysiological data in the presence of volume-conduction, noise and sample-size bias. *NeuroImage* 55:1548–1565.
- Wens V, Marty B, Mary A, Bourguignon M, Op de Beeck M, Goldman S, Van Bogaert P, Peigneux P, De Tiège X (2015) A geometric correction scheme for spatial leakage effects in MEG/EEG seed-based functional connectivity mapping: Spatial Leakage Geometric Correction Scheme. *Human Brain Mapping* 36:4604–4621.

Westner B (2017) High Frequency Oscillations in Healthy Brain Functions Doctoral Thesis, University of Konstanz, Konstanz.

Westner BU, Brookes MJ, Dalal SS (2015) The effect of sensor array density on beamformer performance. In *International Conference on Basic and Clinical Multimodal Imaging*, Utrecht, The Netherlands.

Westner BU, Dalal SS, Gramfort A, Litvak V, Mosher JC, Oostenveld R, Schoffelen JM (2022) A unified view on beamformers for M/EEG source reconstruction. *NeuroImage* 246:118789.

Woolrich M, Hunt L, Groves A, Barnes G (2011) MEG beamforming using Bayesian PCA for adaptive data covariance matrix regularization. *NeuroImage* 57:1466–1479.